Elastic and frictional properties of graphene

Changgu Lee[1], Xiaoding Wei[1], Qunyang Li[2], Robert Carpick[2], Jeffrey W. Kysar[1], and James Hone*,[1]

[1] Mechanical Engineering, Columbia University, New York, NY 10025, USA
[2] Mechanical Engineering, University of Pennsylvania, Philadelphia, PA 19104, USA

* Corresponding author: e-mail jh2228@columbia.edu, Phone: +1 212 854 6244, Fax: +1 212 854 3304

We describe studies of the elastic properties and frictional characteristics of graphene samples of varying thickness using an atomic force microscope. For tensile testing, graphene is suspended over micron-sized circular holes and indented by atomic force microscope (AFM) tips. Fitting of the force-displacement curves yields the prestress and elastic stiffness, while comparison of the breaking force to simulation gives the ultimate strength, which is the highest measured for any material. Experiments on samples with 1–3 atomic layers yield similar values for the intrinsic stiffness and strength of a single sheet, but also reveal differences in mechanical behavior with thickness. The frictional force between an AFM tip and graphene decreases with thickness for samples from 1 to 4 layers, and does not depend on the presence of a substrate. High-resolution friction force imaging in stick-slip mode shows the same trend, and allows direct imaging of the crystal lattice.

1 Introduction Graphene, a one atom thick carbon sheet, forms the basis of both three-dimensional graphite and one-dimensional carbon nanotubes. Graphitic carbon has previously been found to have excellent mechanical properties such as ultra-high strength and low friction coefficient [1–3].

Here we present measurements of the elastic properties and frictional behavior of monolayer and multilayer graphene using atomic force microscopy (AFM) techniques. Elastic properties were measured by AFM nanoindentation and friction was measured by friction force microscopy (FFM), which measures lateral forces during scanning. AFM is a useful tool for the mechanical characterization of graphene for several reasons. It can identify the thickness of a graphene sample easily and accurately using contact mode imaging [4]. It can also resolve the small forces involved in deformation and friction of graphene precisely. Beyond the exploration of graphene's basic mechanical properties, this work demonstrates the utility of AFM in mechanical and structural characterization of atomically thin two-dimensional materials.

2 Elastic properties of graphene

2.1 Experimental procedure and analytical tools In order to measure the elastic properties of graphene, an array of circular wells (diameters 1.5 and 1 μm, depth 500 nm) was patterned onto a Si substrate with a 300 nm SiO_2 epilayer, using nanoimprint lithography and reactive ion etching [Fig. 1(a)]. Graphite flakes were then mechanically exfoliated onto the substrate [5]. Optical microscopy was used to find flakes of monolayer, bilayer, and trilayer graphene, whose thicknesses were confirmed with AFM contact mode imaging [4] and Raman spectroscopy [6]. Figure 1(a) shows a monolayer graphene flake deposited over many circular wells to form a series of freestanding membranes. Non-contact mode AFM imaging [Fig. 1(b)] reveals that the graphene forms a flat membrane which adheres to the vertical wall of the hole for 2–10 nm, presumably due to van der Waals attraction to the substrate.

The elastic properties of the freestanding films were probed by indenting the center of each film using an AFM (XE-100, Park Systems), as illustrated in Fig. 1(c). Because of the strength of the films, cantilevers with diamond tips

Phys. Status Solidi B **246**, No. 11–12 (2009)

Original

Paper

2563
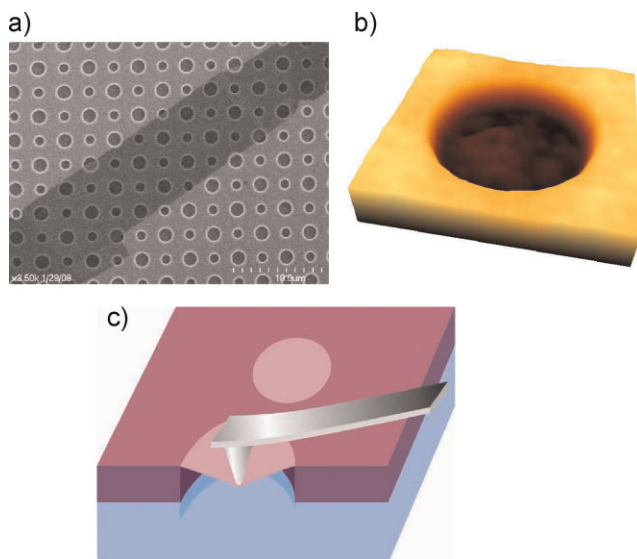
Figure 1 (online colour at: www.pss-b.com) Image of suspended graphene membranes and AFM nanoindentation schematic. (a) Scanning electron micrograph of a large graphene flake spanning an array of circular holes 1 and 1.5 μm in diameter. (b) AFM topography of suspended graphene (the step height in the hole is about 3 nm). (c) Schematic of nanoindentation on suspended graphene membrane.

were used for this study. The tip radii, ranging from ∼15–30 nm, were measured before and after indentation using a transmission electron microscope (TEM). The cantilever spring constants were calibrated against a reference cantilever [7]. Mechanical testing was performed at a constant displacement rate, followed by load reversal. Once the data for elastic properties of the films were recorded, the films were once again indented at the same rate, but this time to failure. The force-displacement data were processed to determine the elastic stiffness and breaking stress of the graphene membranes.

Because of the low defect density in the films, graphene's elastic behavior reflects the intrinsic properties of the interatomic bonding all the way up to the breaking point. Therefore, the response of the graphene must be considered as non-linear since the stress–strain response must curve over to a maximum point that defines the intrinsic breaking stress. Elastic behavior arises from the lowest-order, quadratic, term in the potential energy, while the third-order term gives rise to non-linear elastic behavior [8]. In the simplest model, the resulting isotropic elastic response under uniaxial extension can be expressed as

$$\sigma = E\varepsilon + D\varepsilon^2, \qquad (1)$$

where σ is the stress, ε the strain, E the Young's modulus, and D is the third-order elastic modulus. The value of D is typically negative so the presence of the second order term leads to a lessening of stiffness at high tensile strains and an increasingly stiff response at high compressive strains. E is

determined from components of the second-order fourth-rank stiffness tensor (with two independent components for an isotropic material), while D is determined from components of both the second-order fourth-rank stiffness tensor as well as the third-order sixth-rank stiffness tensor (with three independent components for an isotropic material). Numerical simulations of graphene sheets and nanotubes suggest that a non-linear elastic response is appropriate [9, 10].

In this model, the maximum of the elastic stress–strain response defines the intrinsic stress, which for this functional form is $\sigma_{int} = E^2/4D$ at strain $\varepsilon_{int} = E/2D$, so it remains only to determine E and D from the experimental results. In this work, we determine the value of E based upon the experimental force-displacement data and infer the value of D from the experimental breaking force.

Monolayer graphene is a true two-dimensional material, so its strain energy density is normalized by area of the graphene sheet rather than by volume. Therefore, its behavior under tensile loading is properly described by a two-dimensional strain σ^{2D}, and elastic constants E^{2D} and D^{2D}, with units of force/length. For purposes of comparison to bulk graphite and other materials, these quantities can be divided by the interlayer spacing in graphite ($h = 0.335$ nm [11]) in order to obtain the corresponding three-dimensional parameters.

We first consider the force–displacement behavior of the graphene membranes. Because the tip radius R is much larger than the thickness of the film, bending stiffness can be ignored in the modeling. In addition, because the tip radius is much smaller than the membrane radius a, at most 1% of the graphene film is strained to the point where the non-linear term in Eq. 1 becomes important. Therefore, for the purposes of modeling the force–displacement behavior, the system can be approximated as a clamped circular membrane, made of a linear isotropic elastic material, under central point loading. Isotropic mechanical properties are employed due to the six-fold rotation symmetry of the graphene atomic lattice [12].

Given the above model, the force–displacement behavior can be approximated [13, 14] as

$$F = \sigma_0^{2D}(\pi a)\left(\frac{\delta}{a}\right) + E^{2D}(q^3 a)\left(\frac{\delta}{a}\right)^3, \qquad (2)$$

where F is the applied force, δ the deflection at the center point, σ_0^{2D} the pre-tension in the film, and $q = 1/(1.05 - 0.15\nu - 0.16\nu^2) = 1.02$; and ν is the Poisson's ratio (taken here as 0.165, the Poisson's ratio for graphite in the basal plane [15]). It is therefore possible to extract both the pre-tension and the elastic modulus by fitting the force-displacement curve to Eq. (2).

2.2 Elastic modulus Figure 2 shows typical force-displacement curves for monolayer graphene (a) and bilayer graphene (b). For both samples, the force-displacement behavior is identical on loading and unloading, showing that

a)

b)
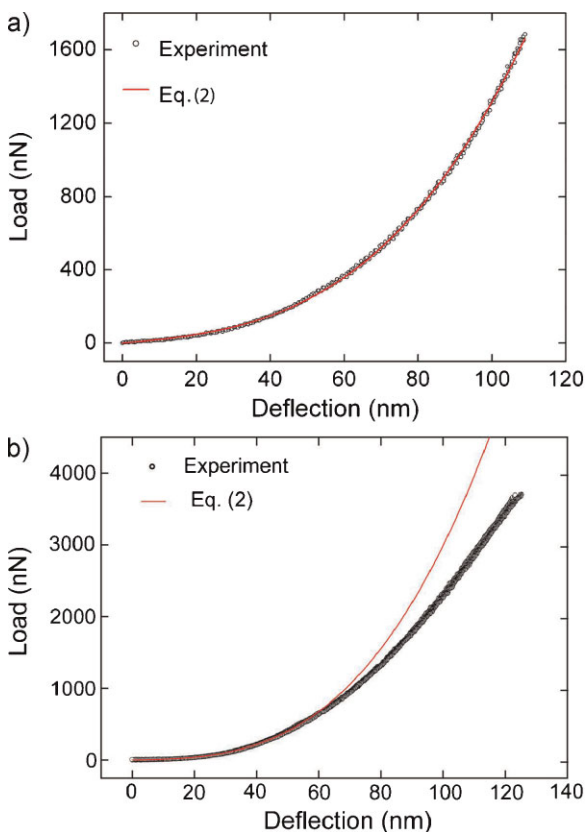
Figure 2 (online colour at: www.pss-b.com) Load/deflection data and curve fitting of Eq. (2): (a) monolayer graphene, (b) bilayer graphene.

there is no slippage or plastic deformation in the samples. For monolayer graphene, the data follow Eq. (2) even up to large displacements. Fitting the results for 67 individual tests yield a mean value of E^{2D} is 342 N/m ($\pm$50 N/m). This value corresponds to a bulk Young's modulus of 1.02 TPa, if the sheet thickness is taken to be the interlayer spacing of bulk graphite (0.335 nm). The elastic modulus values obtained from all data subsets (different flakes, tips, well radii, indentation depth, and indentation speed) were statistically indistinguishable.

As seen in Fig. 2(b), the force-displacement curves for bilayer graphene follow Eq. (2) well up to moderate deflection. However, for displacements larger than ~50 nm, the curves show a softening, and the data falls significantly below the curve obtained by fitting the small-displacement data. While this type of behavior could be caused by slip or plastic deformation, the curves show almost completely elastic response, *i.e.*, identical behavior on loading and unloading. Also the experiment was repeatable regardless of the number of indentations on the same spot, and showed the same behavior on every sample. Therefore, the softening effect in the curves is not from plastic deformation. One possible explanation for the phenomenon is slip between the graphene layers. When the tip indents the multilayer membrane, the slight bending in the membrane

under the tip causes a difference of elongation between the layers. Slip will occur when the elongation difference between the layers is equal to the carbon–carbon bond length, which is about 0.14 nm. A simple model of the strain gradient at the contact boundary between the AFM tip and the membrane shows that this condition is reached at ~50 nm displacement, as observed from our experiments.

To obtain elastic moduli, we fitted the data up to 50 nm of displacement to obtain the second-order elastic modulus of the membranes. The measured moduli for bi and trilayer graphene were 698 and 986 N/m, respectively. These correspond to Young's moduli of $E = 1.04$ and 0.98 TPa, assuming 0.335 nm as the thickness of one layer. Within experimental error, the Young's moduli of monolayer, bilayer, and trilayer graphene are all identical, and equal to the value for bulk graphite.

2.3 Fracture strength The fracture strength of graphene was measured by loading the membranes to the breaking point. The films break at large deflections (above 100 nm), indicating the ability of the material to undergo enormous strains. The force required to break the membranes depends strongly on the tip radius: monolayer films break at forces of about 1.8 μN using a 16.5 nm radius tip, and 2.9 μN using a 27.5 nm tip. The variation in breaking force with tip radius is due to the extreme stress concentration at the tip. This can be modeled in the elastic regime to yield an analytical expression for the breaking strain σ_m as a function of breaking force P and tip radius R:

$$\sigma_m = \left(\frac{PE}{4\pi hR} \right)^{\frac{1}{2}}. \qquad (3)$$

For monolayer films, this model [16] yields an average breaking strength of 55 N/m. However, because the model ignores non-linear elasticity, this value overestimates the strength. To extract the true breaking strain, a series of finite element simulations was performed, using non-linear stress–strain behavior given by Eq. 1. By performing the simulations for various values of the third-order elastic
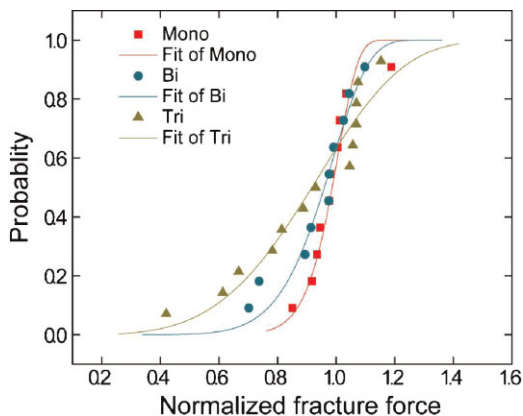
Figure 3 (online colour at: www.pss-b.com) Weibull analysis of graphene of different thicknesses.

Phys. Status Solidi B **246**, No. 11–12 (2009)

2565

modulus D, it was possible to find the value of D that agreed best with experiment. For monolayer films, this value was $D = -680\,N/m$, yielding a two-dimensional ultimate strength of $42\,N/m$, which corresponds to a strength of $\sim 130\,GPa$ in the bulk limit. This value is consistent with predictions of intrinsic strength based upon *ab initio* calculations for monolayer graphene [9, 10].

We have recently repeated these measurements for bilayer and trilayer membranes as well. Because the indentation curves do not follow Eq. (2), it is difficult to find a correct model to extract the fracture strength. To provide a good estimate, we note that the measured fracture strength varies approximately as $R^{1/2}$, consistent with the linear elastic model (Eq. 3). Therefore, we can use the measured strength of monolayer graphene [17], together with the tip radius used in each experiment, to scale the multilayer results. The estimated strength (divided by the effective thickness to give an equivalent bulk strength), which represents an upper bound of the true strength, decreases with the thickness, from $126\,GPa$ for bilayers to $101\,GPa$ for trilayer graphene.

In order to more fully characterize the film failure, we performed Weibull analysis [18] of the statistical distribution of fracture forces. In this analysis, the probablility of fracture at a given force F_f, normalized by the nominal breaking force F_0, is given by:

$$P = 1 - \exp\left[-\left(F_f/F_0\right)^m\right], \tag{4}$$

where m is the Weibull modulus that determines the breadth of the probability distribution. A large value of m indicates a narrow range of defects in the material. Figure 3 shows the Weibull distributions of fracture force for monolayer, bilayer, and trilayer graphene. From this analysis, it is clear that the fracture strength distribution widens with increasing membrane thickness. The Weibull modulus decreases by half for each additional layer, from 15 for monolayers to 4 for trilayers. A possible cause can be the fracture at lower force due to the higher strain on the outer layer. Unlike monolayer graphene, multilayer graphene should have non-uniform strain across the thickness, with the outmost layer having the highest strain. Thus, the distribution of fracture force can be amplified.

3 Frictional characteristics of graphene We next describe AFM-based measurements of friction in monolayer and multilayer graphene. Samples were prepared by the same method described in Section 2. In most cases, the samples were deposited on flat Si/SiO_2 substrates; to examine substrate effects, suspended graphene membranes, similar to those studied in Section 2 but with 300 nm diameter, were also made. The graphene films were then imaged in contact mode using silicon probes. Micron-scale experiments were performed in an ambient environment on an AFM (XE-100, Park systems). Silicon cantilevers with normal force constant of $0.056\,N/m$ (CSC17 from Mikromasch) were used at an applied force of 1 nN. The scan speed varied
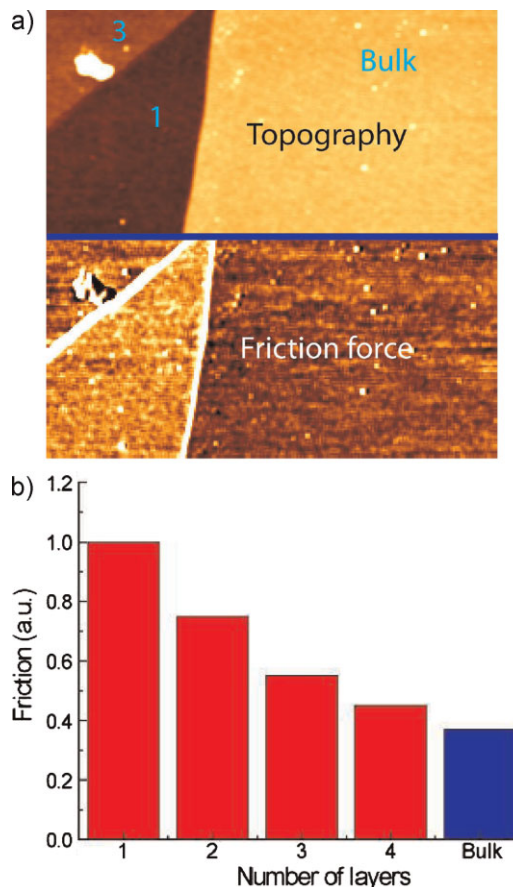
Figure 4 (online colour at: www.pss-b.com) Layer dependence of friction on graphenes. (a) AFM topography and Friction force on graphenes for different thicknesses. (b) Friction chart for different number of layers. The numbers in (a) denote number of layers.

depending on the image size and ranged from 1 to 10 μm/s. Friction force was obtained by dividing the friction signal difference between forward and reverse scans by two.

The top image in Fig. 4(a) shows a topography image of a sample containing areas with 1, 3, and bulk graphene layers. As expected, the thickness difference is ~ 0.3–0.4 nm between each layer. The corresponding FFM image [Fig. 4(a), bottom] shows clear contrast in friction signal between the different thicknesses, but with opposite contrast: the thinner areas show the largest friction. Figure 4(b) shows the compiled results from five samples, including a ~ 100 nm thick flake to represent bulk graphite. The friction force decreases monotonically with sample thickness, and converges to that of bulk graphite as the number of layers increases above ~ 5.

The trend of decreasing friction with increasing number of layers did not depend on scan speed (from 1 to 10 μm/s), and was repeatable over five different samples. Varying the applied load from 0.1 to 2 nN did not produce any significant change in friction. Friction forces can vary with tip size, shape, and composition, applied load, environment, and scan speed. In our experiments, these factors are all kept constant

for a given sample, and therefore we report the friction normalized to the value measured for monolayer graphene on each sample. However, the magnitude of the measured friction forces did not vary appreciably. We also measured the adhesion force between the tip and graphene flakes with different number of layers and found that there was virtually no difference between different thicknesses. We also measured friction on suspended graphene membranes and found that there is no difference between suspended and supported graphene.

To interrogate this behavior further, we measured the atomic-scale frictional behavior at much smaller length scales. These experiments were carried out in a dry nitrogen purged chamber using an RHK UHV300 AFM, where relative humidity was measured to be <10% and based on measurements of similar conditions is likely ∼1–2%. For these measurements the silicon cantilever had a force constant of 0.18 N/m (CSC37, from Mikromasch) and the applied force was maintained at 4 nN for all measurements. The scan speed was 40 nm/s for 2 nm scan sizes and 100 nm/s for 5 nm scan sizes. Because of the lateral force variations that occur during stick-slip behavior, the relative frictional force was obtained by integrating the friction signal over forward and reverse scans and calculating the difference of the two integrals, and normalizing the result by the value obtained for monolayer graphene.

The tip exhibited clear, periodic stick-slip motion when sliding over the graphene as shown in Fig. 5(a). This behavior is similar to that reported previously for bulk graphite [19, 20], and was observed for all graphene layers. The stick-slip image reveals the graphene lattice, and such imaging may be useful for determining the lattice orientation of graphene on insulating substrates, where other techniques such as scanning tunnelling microscopy are more difficult. The frictional energy dissipated within 2 and 5 nm friction loops is plotted in Fig. 5(b) for as a function of the sample thickness. The energy dissipation decreases monotonically as the number of graphene layers increases, and approaches that of bulk graphite, consistent with the micrometer-scale measurements in ambient conditions.

After ruling out substrate effects and influence of adhesion, we conclude that the layer-dependence of friction appears to be governed by dissipation mechanisms taking place at the tip-graphene interface. One possible explanation can be the bending of graphene while the AFM slides across it. Recently, suspended graphene has been found to have ripples due to its low bending rigidity, whose sizes are around 5–10 nm and heights ∼1 nm for monolayers [21–24]. Due to the size of AFM tips (tip radius ∼10 nm), it was difficult to identify ripples in suspended and supported grapheme. However, it is possible that either suspended or substrate-mounted graphene films can bulge out and an extended area can snap into contact with the tip due to tip-graphene adhesion. When the tip slides, besides the energy required to overcome the local tip-graphene interfacial potential recognized as the source of regular stick-slip motion [25], extra energy is needed to push the bulging ripples forward. This
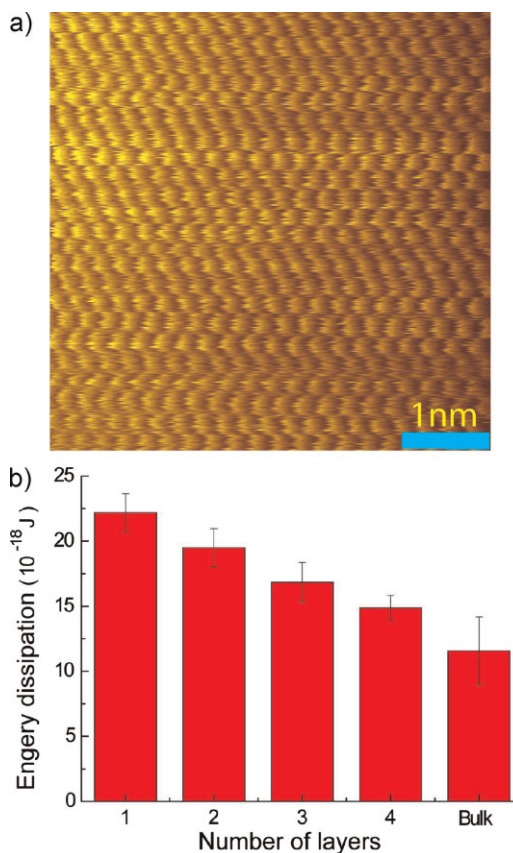
Figure 5 (online colour at: www.pss-b.com) Atomic scale friction measurement using stick-slip mode. (a) A typical atomic stick-slip FFM image on four layer graphene showing the three-fold symmetric lattice pattern. (b) Energy dissipation due to friction within 5 nm reciprocal scans on surfaces with different graphene layers as well as bulk graphite.

extra energy dissipation due to this ''rippling-rug effect'' can lead to higher frictional resistance and it should decay as the graphene becomes thicker and stiffer. In order to validate this idea, more systematic measurement of atomic scale friction on graphene with various thicknesses needs to be conducted, and proper mechanical models have to be established.

Filleter et al. [26] recently reported similar results for graphene epitaxially grown on a SiC substrate. They suggest that electron–phonon coupling, as observed by angle-resolved photonemission, is the cause of the phenomenon. However, it is difficult to generalize their explanation because the substrate may strongly affect the coupling. Collectively, their observation along with ours shows that the effect occurs regardless of substrate (SiO_2, SiC, suspended).

4 Conclusions Two AFM techniques, nanoindentation and FFM, enable us to measure elastic properties and frictional characteristics of graphene. The second-order elastic modulus agrees well with predictions by *ab initio* calculations [27]. Also, the third-order modulus and intrinsic strength can be measured by the current method due to the

Original

Paper

Phys. Status Solidi B **246**, No. 11–12 (2009)   2567

almost defect-free state of monolayer graphene. The measurement is possible because the area under high strain is concentrated near the AFM tip, and is therefore unlikely to have defects. Friction forces measured on mechanically exfoliated graphene decrease with thickness. Our observations exclude substrate effects, adhesion force variation, scan rate, and load as possible explanations for the decrease in friction with increasing thickness. A rippling-rug effect is proposed as a possible explanation for this phenomenon. We are conducting more experiments and theoretical investigations to test this hypothesis.

References

[1] B. Peng, M. Locascio, P. Zapol, S. Li, S. L. Mielke, G. C. Schatz, and H. D. Espinosa, Nature Nanotechnol. **3**, 626 (2008).

[2] U. D. Schwarz, O. Zwörner, P. Köster, and R. Wiesendanger, Phys. Rev. B **56**, 6987 (1997).

[3] M.-F. Yu, O. Lourie, M. J. Dyer, K. Moloni, T. F. Kell, and R. S. Ruoff, Science **287**, 637 (2000).

[4] P. Nemes-Incze, Z. Osváth, K. Kamarás, and L. P. Biró, Carbon **46**, 1435 (2008).

[5] K. S. Novoselov, D. Jiang, F. Schedin, T. J. Booth, V. V. Khotkevich, S. V. Morozov, and A. K. Geim, Proc. Natl. Acad. Sci. USA **102**, 10451 (2005).

[6] A. C. Ferrari, J. C. Meyer, V. Scardaci, C. Casiraghi, M. Lazzeri, F. Mauri, S. Piscanec, D. Jiang, K. S. Novoselov, S. Roth, and A. K. Geim, Phys. Rev. Lett. **97**, 187401 (2006).

[7] M. Tortonese and M. Kirk, Proc. SPIE **3009**, 53 (1997).

[8] R. N. Thurston and K. Brugger, Phys. Rev. **133**, A1604 (1964).

[9] F. Liu, P. M. Ming, and J. Li, Phys. Rev. B **76**, (2007).

[10] K. Roopam, L. M. Steven, T. P. Jeffrey, Z. Sulin, B. Roberto, C. S. George, and B. Ted, Phys. Rev. B **75**, 075412 (2007).

[11] R. Al-Jishi and G. Dresselhaus, Phys. Rev. B **26**, 4514 (1982).

[12] J. F. Nye, Physical Properties of Crystals (Oxford University Press, USA, 1985).

[13] K.-T. Wan, S. Guo, and D. A. Dillard, Thin Solid Films **425**, 150 (2003).

[14] U. Komaragiri, M. R. Begley, and J. G. Simmonds, J. Appl. Mech. **72**, 203 (2005).

[15] O. L. Blakslee, J. Appl. Phys. **41**, 3373 (1970).

[16] N. M. Bhatia and W. Nachbar, Int. J. Non-lin. Mech. **3**, 307 (1968).

[17] C. Lee, X. Wei, J. W. Kysar, and J. Hone, Science **321**, 385 (2008).

[18] B. Lawn, Fracture of Brittle Solids, second ed. (Cambridge University Press, Cambridge, 1993).

[19] C. M. Mate, G. M. McClelland, R. Erlandsson, and S. Chiang, Phys. Rev. Lett. **59**, 1942 (1987).

[20] S. N. Medyanik, W. K. Liu, I.-H. Sung, and R. W. Carpick, Phys. Rev. Lett. **97**, 136106 (2006).

[21] J. C. Meyer, A. K. Geim, M. I. Katsnelson, K. S. Novoselov, T. J. Booth, and S. Roth, Nature **446**, 60 (2007).

[22] S. V. Morozov, K. S. Novoselov, M. I. Katsnelson, F. Schedin, L. A. Ponomarenko, D. Jiang, and A. K. Geim, Phys. Rev. Lett. **97**, 016801 (2006).

[23] M. Ishigami, J. H. Chen, W. G. Cullen, M. S. Fuhrer, and E. D. Williams, Nano Lett. **7**, 1643 (2007).

[24] A. Fasolino, J. H. Los, and M. I. Katsnelson, Nature Mater. **6**, 858 (2007).

[25] G. A. Tomlinson, Philos. Mag. **7**, 905 (1929).

[26] T. Filleter, J. L. McChesney, A. Bostwick, E. Rotenberg, K. V. Emtsev, S. Th, K. Horn, and R. Bennewitz, Phys. Rev. Lett. **102**, 086102 (2009).

[27] F. Liu, P. Ming, and J. Li, Phys. Rev. B **76**, 064120 (2007).